A&A 470, 269–279 (2007)
DOI: 10.1051/0004-6361:20077094

Astronomy & Astrophysics

A jet-like outflow toward the high-mass (proto) stellar object IRAS 18566+0408

Q. Zhang[1], T. K. Sridharan[1], T. R. Hunter[2], Y. Chen[1], H. Beuther[3], and F. Wyrowski[4]

[1] Harvard-Smithsonian Center for Astrophysics, 60 Garden Street, Cambridge, Massachusetts 02138, USA
e-mail: qzhang@cfa.harvard.edu
[2] National Radio Astronomical Observatory, 520 Edgemont Road, Charlottesville, VA 22903-2475, USA
[3] Max-Planck-Institute for Astronomy, Königstuhl 17, 69117 Heidelberg, Germany
[4] Max-Planck-Institut für Radioastronomie, Auf dem Hugel 69, 53121 Bonn, Germany

Received 12 January 2007 / Accepted 11 April 2007

ABSTRACT

Context. Studies of high-mass protostellar objects reveal important information regarding the formation process of massive stars.
Aims. We study the physical conditions in the dense core and molecular outflow associated with the high-mass protostellar candidate IRAS 18566+0408 at high angular resolution.
Methods. We performed interferometric observations in the NH_3 $(J, K) = (1, 1), (2, 2)$ and (3,3) inversion transitions, the SiO $J = 2$–1 and HCN $J = 1$–0 lines, and the 43 and 87 GHz continuum emission using the VLA and OVRO.
Results. The 87 GHz continuum emission reveals two continuum peaks MM-1 and MM-2 along a molecular ridge. The dominant peak MM-1 coincides with a compact emission feature at 43 GHz, and arises mostly from the dust emission. For dust emissivity index β of 1.3, the masses in the dust peaks amount to 70 $M_\odot$ for MM-1, and 27 $M_\odot$ for MM-2. Assuming internal heating, the central luminosities of MM-1 and MM-2 are 6×10^4 and 8×10^3 $L_\odot$, respectively.
The SiO emission reveals a well collimated outflow emanating from MM-1. The jet-like outflow is also detected in NH_3 at velocities similar to the SiO emission. The outflow, with a mass of 27 $M_\odot$, causes significant heating in the gas to temperatures of 70 K, much higher than the temperature of $\lesssim$15 K in the extended core. Compact (<3″) and narrow line (<1.5 km s^{-1}) NH_3 (3,3) emission features are found associated with the outflow. They likely arise from weak population inversion in NH_3 similar to the maser emission.
Toward MM-1, there is a compact NH_3 structure with a linewidth that increases from 5.5 km s^{-1} *FWHM* measured at 3″ resolution to 8.7 km s^{-1} measured at 1″ resolution. This linewidth is much larger than the *FWHM* of <2 km s^{-1} in the entire core, and does not appear to originate from the outflow. This large linewidth may arise from rotation/infall, or relative motions of unresolved protostellar cores.

Key words. ISM: kinematics and dynamics – ISM: H II regions – ISM: clouds – masers – ISM: jets and outflows – stars: formation

1. Introduction

Systematic surveys in the past decade identified hundreds of high-mass protostellar candidates (Molinari et al. 1996; Sridharan 2002; Fontani et al. 2005). These objects, selected initially from the IRAS point source catalog, typically have far infrared luminosities of $\gtrsim 10^3$ $L_\odot$, contain 10^2–10^4 $M_\odot$ of dense molecular gas (Molinari et al. 2002; Beuther et al. 2002a; Williams et al. 2004; Beltrán et al. 2006), and are associated with massive molecular outflows (Zhang et al. 2001, 2005; Beuther et al. 2002b). Compared with ultra compact HII (UCHII) regions, high-mass protostellar candidates have similar amounts of dense molecular gas, but are less luminous and have much weaker emission at centimeter wavelengths. Therefore, they are likely to be in an earlier evolutionary stage than the UCHII phase.

These surveys were carried out mostly using single dish telescopes with angular resolutions of >10″. High angular resolution imaging is required to probe dense cores and molecular outflows at spatial scales relevant to massive protostars. In the past few years, images from (sub)mm interferometers have often resolved poorly-collimated outflows identified by single dish telescopes into multiple well-collimated outflows (e.g. IRAS 05358+3543, Beuther et al. 2002d; AFGL 5142, Zhang et al. 2007). In the meantime, high resolution images in NH_3 and other dense molecular gas tracers reveal interesting kinematics close to massive protostars (Zhang et al. 1998, 2002).

In this paper, we present a high resolution study toward the high-mass protostellar candidate IRAS 18566+0408. At a kinematic distance of 6.7 kpc (Sridharan et al. 2002), the source has a far infrared luminosity of several 10^4 $L_\odot$. The object was initially undetected at 2 and 6 cm at an rms of 0.16 mJy and 0.1 mJy, respectively (Miralles et al. 1994), but later detected at 3.6 cm at a flux density of 0.7 mJy (Carral et al. 1999), and at 2 cm at a flux of 0.7 mJy (Araya et al. 2005).

This region is associated with H_2O maser emission at 22 GHz, CH_3OH maser emission at 6.7 GHz, and H_2CO maser emission at 8 GHz (Miralles et al. 1994; Slysh et al. 1999; Beuther et al. 2002c; Araya et al. 2005). Dense gas traced by CS and CH_3CN, as well as (sub)mm continuum emission is observed (Bronfman et al. 1996; Sridharan et al. 2002; Beuther et al. 2002a; Williams et al. 2004). NH_3 (1,1) and (2,2) emission was detected first by Miralles et al. (1994), and also by Molinari et al. (1996) (source 83) and Sridharan et al. (2002) with single dish telescopes.

Beuther et al. (2002b) report a CO outflow in the northwest-southeast direction. The geometric center of the outflow, however, is about 10″ north of the 1.2 mm emission peak. Since the 1.2 mm continuum position is consistent with that of the submm

Table 1. List of observational parameters.

Instrument	Date of Observations	Line	Bandwidth (MHz)	Spectral Res. (km s^{-1})	Integration Time (h)
VLA-CnB	2001/07/23	NH_3 (1, 1), (2, 2)	3.12	0.6	0.7
VLA-DnC	2001/10/01	NH_3 (3, 3)	3.12	0.3	1.0
VLA-CnB	2002/09/26	NH_3 (1, 1), (2, 2)	3.12	0.6	1.2
VLA-CnB	2002/09/26	NH_3 (3, 3)	3.12	0.6	1.0
VLA-CnB	2002/09/26	23 GHz	25	-	1.0
VLA-DnC	2003/01/16	NH_3 (1, 1), (2, 2)	3.12	0.3	0.6
VLA-DnC	2003/01/24	NH_3 (3, 3)	3.12	0.6	1.0
VLA-DnC	2003/02/04	43 GHz	50	-	2
OVRO-E	2002/11/02	HCN (1, 0)	30	3.4	4.0
OVRO-E	2002/11/02	SiO (2–1)	30	1.7	4.0
OVRO-E	2002/11/02	HCO^+ (1–0)	7.5	0.84	4.0
OVRO-E	2002/11/02	87 GHz	4000	-	4.0
OVRO-H	2002/12/01	87 GHz	4000	-	2.0

emission (Williams et al. 2004), this offset is possibly caused by pointing problems in the CO observations with the IRAM 30 telescope (Beuther H., private communication). The 1.2 mm emission shows an extension of 15″ toward the northwest of the peak emission. SiO J = 2–1 emission is detected in the region with a linewidth of 30 km s^{-1} at zero intensity (Beuther H., private communication).

The high resolution observations with the VLA and OVRO in this paper reveal a collimated outflow in SiO and kinematics in the dense core. In Sect. 2, we describe details of observations. In Sect. 3, we present the main observational results. In Sect. 4, we discuss the different kinematic components in the region. A summary is given in Sect. 5.

2. Observations

2.1. VLA

2.1.1. NH_3 observations

The VLA[1] observations of IRAS 18566+0408 were first conducted on 2001 July 23 in the NH_3 (J, K) = (1, 1) and (2, 2) lines in the C configuration. To improve the S/N in the data, follow-up observations were made from 2001 October to 2003 January, in both CnB and DnC configurations in the NH_3 (1, 1), (2, 2) and (3, 3) inversion transitions. The integration time on source was typically less than 1 h for each line. The pointing center of the observations was RA (2000) = $18^h59^m09^s.88$ and Dec (2000) = +04°12′13″.6. We used 1849+005, 3C 286 and 3C 273 as the gain, flux, and bandpass calibrators. The detailed parameters of the observations are summarized in Table 1.

The visibility data were calibrated using the NRAO Astronomical Image Processing System (AIPS). The uncertainty in the flux calibration is about 10%. The calibrated visibilities from different epochs were combined for the same line and imaged in MIRIAD. The rms noise in the (1, 1), (2, 2) and the (3, 3) lines is about 2 mJy in a 3″ to 4″ synthesized beam per 0.6 km s^{-1} wide channel.

2.1.2. 23 GHz and 43 GHz continuum

The continuum observations at 23 GHz and 43 GHz were carried out with the VLA on 2002 September 26 and 2003 February 04, respectively. At 43 GHz, we used the fast switching calibration scheme that alternated between IRAS18566+0408 and the gain calibrator 1849+005 in a cycle of 2 min. The total on-source time for IRAS18566+0408 was about 2 h at 43 GHz, and 1 h at 23 GHz. Calibration and imaging were performed in AIPS. The flux calibration was done by comparing to 3C 286. The absolute flux scales are accurate to about 10%. The rms is 0.1 mJy in the 43 GHz image, and 0.14 mJy in the 23 GHz image, respectively.

[1] The National Radio Astronomy Observatory is operated by Associated Universities, Inc., under cooperative agreement with the National Science Foundation.

2.2. OVRO

The OVRO observations of IRAS 18566+0408 were carried out during 2002 November to December. The SiO J = 2–1 (v = 0), HCN J = 1–0 and HCO^+ J = 1–0 lines were observed simultaneously in the lower sideband, along with 87 GHz continuum. The SiO line was observed with a total bandwidth of 31 MHz and a spectral resolution of 0.5 MHz (1.7 km s^{-1}). The HCN line was observed with a bandwidth of 30 MHz at a resolution of 1 MHz (3.4 km s^{-1}). The HCO^+ line was observed with a bandwidth of 7.5 MHz at a resolution of 0.25 MHz (0.8 km s^{-1}). In addition, the analog correlator provided continuum measurements of 4 GHz bandwidth. The pointing center of the OVRO observations was the same as that of the VLA observations. The detailed parameters of the observations are summarized in Table 1.

The visibility data were calibrated in the OVRO MMA package and exported to MIRIAD for imaging. The rms is 17 mJy per 1.7 km s^{-1} channel for the line images, and 0.5 mJy for the continuum. The HCO^+ emission is extended and suffers missing short spacing fluxes, thus, is not presented in this paper.

3. Results

3.1. Continuum emission

No emission is detected at 23 GHz at a 1σ rms of 0.14 mJy. Figure 1 presents images of continuum emission at 43 GHz (or 7.0 mm) and 87 GHz (or 3.4 mm). The 43 GHz emission shows a compact feature with the peak position at RA (2000) = $18^h59^m09^s.99$, Dec (2000) = 04°12′15″.7. The emission appears to be slightly resolved with the 2″.7×1″.3 beam at a position angle of −7.6°. The peak and integrated flux densities are 1 mJy/beam and 1.7 mJy, respectively, with a 1σ error of 0.1 mJy. The emission has an extension in the northeast-southwest direction, which appears to be different from the position angle of the beam. The deconvolved size of the emission is 2″.0 × 1″.2 with a position

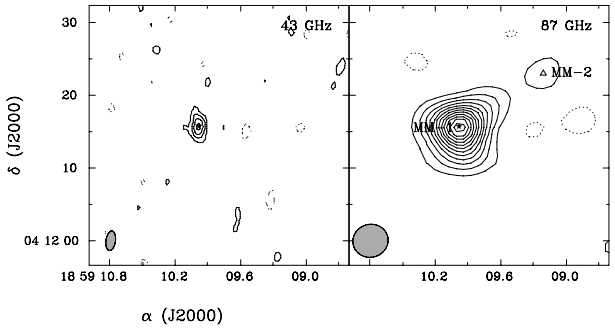

Fig. 1. Continuum emission at 43 GHz and 87 GHz toward IRAS 18566+0408. The contour levels are in steps of 0.25 mJy/beam for the 43 GHz continuum image, and 1.5 mJy/beam for the 87 GHz continuum image. The "star" symbol and "triangle" mark the continuum peaks MM-1 and MM-2, respectively. The size of the synthesized beam is marked by the shaded ellipse at the lower-left corner of each panel.

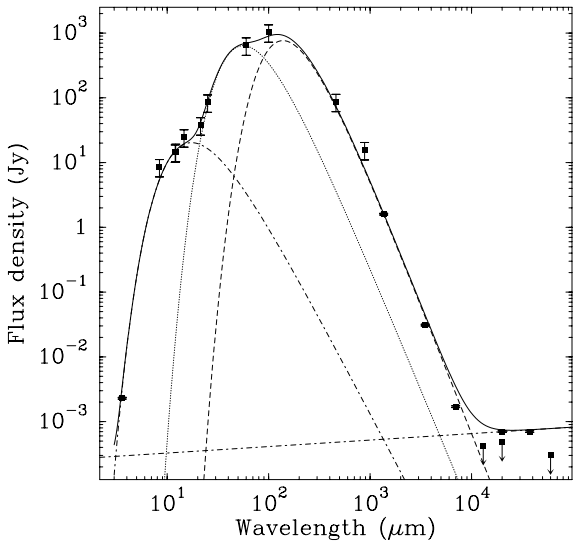

Fig. 2. The spectral energy distribution of IRAS 18566+0408. The dashed line represents a cold dust component, the dotted line represents the warm dust component, the dash-dot line represents the free-free emission, and the solid line represents the sum of all three components.

angle of 24°. This corresponds to a size along the major axis of 1.3×10^4 AU.

The 87 GHz emission is resolved with a $4\farcs9 \times 4\farcs5$ beam using natural weighting. The emission consists of a dominant peak, MM-1, coincident with the peak of the 43 GHz emission to better than $0\farcs1$, and a secondary peak, MM-2, at RA (2000) = $18^{\rm h}59^{\rm m}09\fs21$, Dec (2000) = $04°12'22\farcs6$. The peak flux density of MM-1 is 18 mJy/beam, with an integrated flux density of 31 mJy. MM-2 is much weaker, with a peak flux density of 2.6 mJy/beam. The uncertainty in these measurements is about 15%. There appears to an extented filament at a position angle of −58° connecting MM-1 and MM-2, which is better seen in the lower resolution (11″) 1.2 mm map in Beuther et al. (2002a).

Figure 2 shows the spectral energy distribution of the continuum peak MM-1. The 1.3 cm 3σ upper limit (1σ = 0.14 mJy) is from this paper. The 3.6 cm continuum detection is from Carral et al. (1999). The 2 cm and 6 cm data are from Miralles et al. (1994) and Araya et al. (2005). The 1.2 mm, 850 μm and 450 μm measurements are from the IRAM 30-m telescope and JCMT (Beuther et al. 2002c; Williams et al. 2004). The mid to far infrared data are from IRAS, MSX and Spitzer IRAC measurements.

For emission at longer cm wavelengths, the contribution from dust is negligible. Toward MM-1, a faint continuum source was detected at 2 cm (0.7 mJy) by Araya et al. (2005), and at 3.6 cm (0.7 mJy) by Carral et al. (1999). However, we fail to detect the source at 1.3 cm at an angular resolution of 1″ and a 1σ rms of 0.14 mJy. The detections by Araya et al. (2005) and Carral et al. (1999) were made at resolutions of a few arcseconds, and can be reconciled with the non detection in this paper if the source is more extended than 1″. However, an inconsistency remains at 2cm at which Miralles et al. (1994) failed to detect the source with a 1σ rms of 0.16 mJy at a resolution of 5″. A possible reconciliation is that the flux varies with time. Despite the apparent differences, the faintness of the cm emission indicates that the massive star in this region is still extremely young in its evolution, and has not produced significant free-free emission.

The measurements from wavelengths shortward of 1.2 mm have poorer spatial resolution and sample a much larger area in the region. We fit a greybody model to the entire spectral energy distribution from radio to infrared (IR) wavelengths. The far-IR measurements have a typical resolution of ∼1′. The overall spectral energy distribution can be fitted by three dust components, with temperatures of 210, 58 and 30 K, respectively. The total luminosity of the region determined mainly by mid to far IR data at ∼1′ resolution is $8 \times 10^4\ L_\odot$. The fluxes at the mm and submm wavelengths give a spectral index α of 3.9, defined as $F_\nu \propto \nu^\alpha$, or $\beta = 1.9$.

For the compact continuum source MM-1, we use the high resolution 7 mm and 3 mm data to derive a power law index more appropriate for a mass estimate. To minimize the difference in beam size between the two frequencies, we image the 87 GHz data with a uniform weighting of the visibilities and obtain a peak flux density of 10 mJy/beam with a $3\farcs3 \times 2\farcs0$ beam. These two values (10 and 1.0 mJy/beam) produce an upper limit to the spectral index α of 3.3, or an upper limit to the emissivity index β of 1.3. Assuming that the dust reaches an equilibium with the gas through collision at this high density environment (Burke & Hollenbach 1983), we approximate the dust temperature by the gas kinetic temperature of 80 K measured in NH_3 (see Sects. 3.2, 3.3 and 4.1). For a dust opacity law $\kappa \propto \nu^\beta$, and $\kappa(250\ \mu{\rm m})$ = 12 cm^2 g^{-1} from Hildebrand (1983), we obtain a mass within the $4\farcs9 \times 4\farcs5$ beam (∼30 000 AU) of 70 $M_\odot$ for $\beta = 1.3$. This mass is a small fraction of the mass ($2 \times 10^3\ M_\odot$) estimated from the 1.2 mm emission for the entire region (Beuther et al. 2002a).

For the continuum peak MM-2, the non detection at 7 mm gives a 3σ upper limit of 0.3 mJy. This value and the peak flux density of 2.6 mJy/beam at 87 GHz yield a spectral index of $\gtrsim$3. Using assumptions similar to those for MM-1, we estimate the mass in the MM-2 core. With a temperature of 30 K derived from the NH_3 emission, we obtain a mass of 27 $M_\odot$ for $\beta = 1.3$, and 13 $M_\odot$ for $\beta = 1$.

3.2. Line emission

Figure 3 presents the integrated emission of the NH_3 (J, K) = (1, 1), (2, 2), (3, 3) lines obtained from the VLA, and the SiO J = 2–1 and HCN J = 1–0 transitions obtained from OVRO. In the NH_3 (1, 1) and (2, 2) lines, there appears to be extended emission in the northwest-southeast direction over a scale of 40″. This component is relatively cold as the (2, 2) emission is less extended than the (1, 1) line. MM-2 is associated with NH_3 gas and lies in a molecular ridge connecting MM-1 and MM-2 that is also seen in the dust emission. In addition to the extended

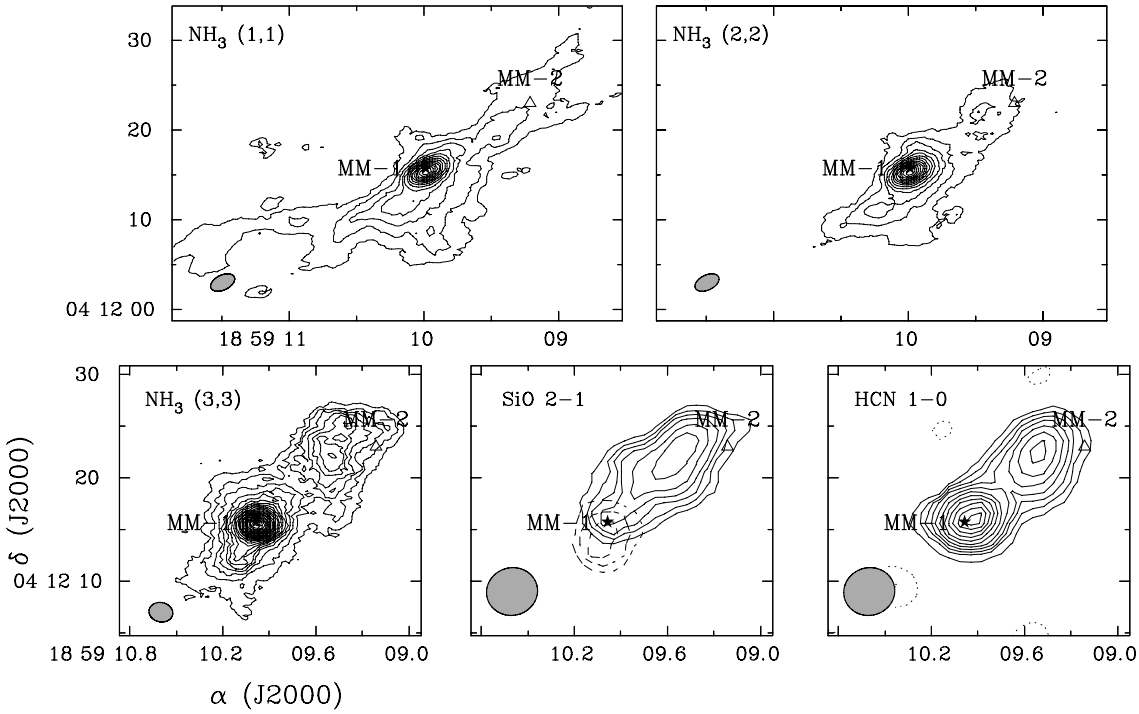

Fig. 3. The integrated emission of the NH_3 $(J, K) = (1, 1), (2, 2), (3, 3)$, SiO $J = (2–1)$, HCN $J = (2–1)$ lines. The velocity range of the integration is 81 to 88 km s^{-1} for the NH_3 (1, 1) and (2, 2) lines. The NH_3 (3, 3) and HCN lines are integrated over the entire spectral line. For the SiO line, the blue-shifted emission (solid contours) is integrated from 50 to 83 km s^{-1} and the red-shifted emission (dashed contours) is integrated from 88 to 110 km s^{-1}. The NH_3 images are made from the VLA-D and C configuration data. The SiO and HCN data images are made from the OVRO E configuration data. The contour levels are in steps of 0.015 Jy km s^{-1} for the NH_3 (1, 1) and (2, 2) lines, 0.02 Jy km s^{-1} for the NH_3 (3,3), 0.3 Jy km s^{-1} for the SiO (2–1), and 0.6 Jy km s^{-1} for the HCN (1–0). The "star" symbol and "triangle" mark the continuum peaks MM-1 and MM-2, respectively. The beam sizes are plotted at the lower-left corner of each panel.

gas component, a compact NH_3 emission component associated with MM-1 is seen in all three NH_3 lines, with a deconvolved size of 1.″2. The peak intensity of the integrated emission in the (2, 2) line is 0.22 Jy km s^{-1}/beam, similar to the value in the (1, 1) line. Thus the gas in this component is relatively warm. In the NH_3 (3, 3) line, there is also extended emission in the northwest-southeast orientation. The extension, at a position angle of 135°, is similar to the emission in SiO and HCN. Unlike in the case of the NH_3 (1, 1) and (2, 2) emission, MM-2 is located toward the edge of the NH_3 (3, 3), SiO and HCN emission.

To show detailed kinematics in the region, Fig. 4 presents the channel maps of the NH_3 $(J, K) = (1, 1), (2, 2)$ and (3, 3) lines. The extended emission is present mostly at velocities from 84 to 87 km s^{-1}, with a peak velocity of 85.2 km s^{-1} corresponding to the cloud systemic velocity (Bronfman et al. 1996). The typical linewidth for the extended emission is about 1–2 km s^{-1} in *FWHM* and the typical temperature is <15 K (see the temperature map in Fig. 6 and discussions in Sect. 4). The relatively narrow linewidth and low temperature in the gas indicate that this extended component is from the quiescent gas in the core.

At velocities of 86 to 87 km s^{-1}, there appears to be a molecular ridge (position angle of 148°) between MM-1 and MM-2 in the (1, 1) and (2, 2) emission. MM-2 coincides with a peak in the NH_3 emission (see channel 86.4 km s^{-1}). At velocities less than 84 km s^{-1} and greater than 87 km s^{-1}, there appears to be compact NH_3 emission toward the position of MM-1. This compact emission, with a *FWHM* of 5.5 km s^{-1} measured at 3″ resolution, is strong in the (2, 2) emission relative to the (1, 1) emission, indicating that the NH_3 gas is rather warm. The ratio of the NH_3 (1, 1) and (2, 2) lines gives a rotational temperature of 45 K.

In the NH_3 (3, 3) line, the extended component seen in the (1, 1) and (2, 2) is not as dominant. A compact emission component toward the position of MM-1 stands out prominently. Since the (3, 3) transition has a higher upper energy level (124 K) as compared to the (1, 1) (23 K) and (2, 2) (65 K) lines, the (3, 3) emission confirms that the compact component is rather warm.

In addition to the compact component toward MM-1, there appear to be four additional compact emission components in the NH_3 (3, 3) line, two toward the east of MM-1 in the velocity channels of 84.6 and 85.5 km s^{-1}, one to the west of MM-1 in the velocity channel of 85.2 km s^{-1}, and one to the northwest of MM-1 from velocities of 85.5 to 85.8 km s^{-1}. We refer to these features as "A", "B", "C" and "D", respectively (the crosses in the channel maps in Fig. 4). There appear to be no corresponding emission peaks in the NH_3 (1, 1) and (2, 2) lines. Unlike the broad NH_3 (3, 3) line emission toward MM-1, these four components have rather narrow velocity width of about 1.5 km s^{-1} in *FWHM*, but extended line wing emission. We will discuss these features further in Sect. 4.

Besides the compact emission components in Fig. 4c, the NH_3 (3, 3) emission also shows an extended structure in the southeast-northwest direction. This structure has rather broad line wings (15 km s^{-1} from the cloud velocity), and high temperatures of 70 K. MM-2 is not associated with any peaks of the (3, 3) emission.

Figure 5a presents the channel maps of the SiO $J = 2–1$ transition. The SiO emission is elongated and lies mostly to the northwest of MM-1 at a position angle of 135°, similar to the extended emission in the NH_3 (3, 3) line. The SiO emission is present from velocities of 70 to 93 km s^{-1}. There appears to

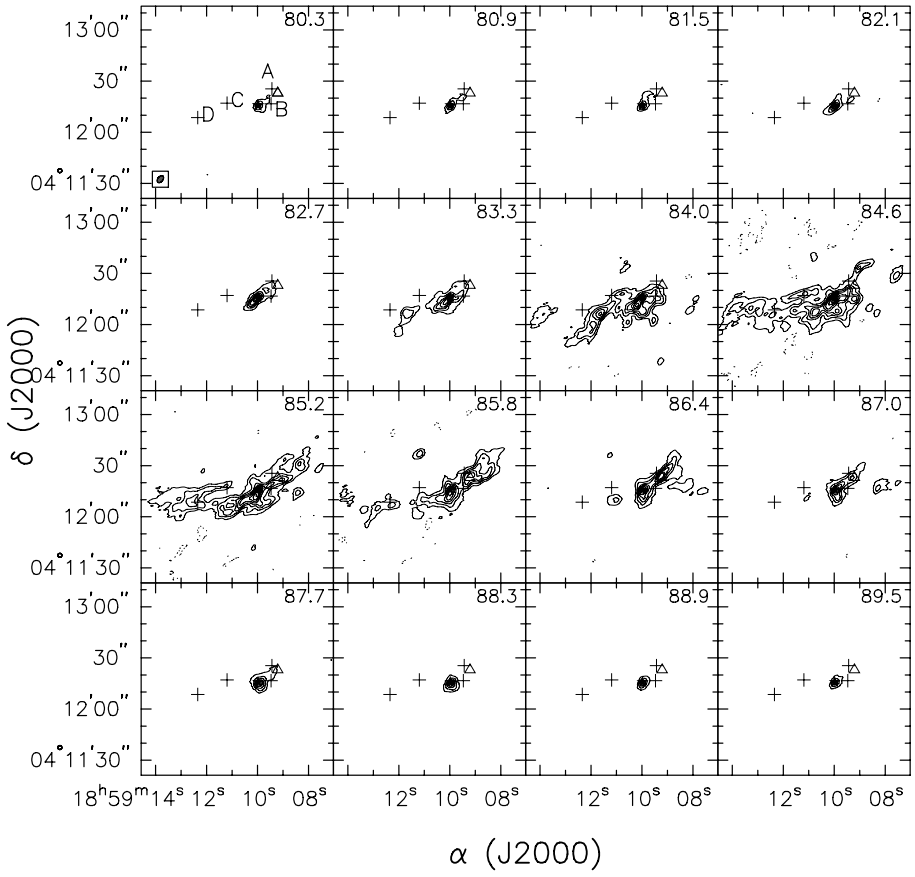

Fig. 4a. The channel maps of the NH_3 $(J, K) = (1, 1)$ (Fig. 4a), $(2, 2)$ (Fig. 4b) and $(3, 3)$ (Fig. 4c) lines. The images were made using the VLA-D configuration data only. The contour levels are in steps of 8 mJy/beam ($\sim 4\sigma$) for the NH_3 (1, 1) and (2, 2) lines and in steps of 9 mJy/beam ($\sim 3\sigma$) for the (3, 3) line. The beam sizes are plotted at the lower-left of the first panel. The velocity of the channel is plotted at the upper-right of each panel. The (1, 1) and (2, 2) images have a spectral resolution of 0.6 km s^{-1}, while the (3, 3) images have a spectral resolution of 0.3 km s^{-1}. The "star" symbol and "triangle" mark the continuum peaks MM-1 and MM-2, respectively. The crosses mark the position of the hot NH_3 (3, 3) features.

be higher velocity SiO emission toward MM-1, but none toward MM-2. Since SiO abundance is typically low in quiescent clouds (Ziurys et al. 1989) and is enhanced by a few orders of magnitude in outflows (e.g. Zhang et al. 1995) due to shock processes (Pineau des Forêts et al. 1997), the SiO emission here most likely traces a well collimated outflow originated from MM-1. The orientation of the SiO outflow is consistent with the bipolar CO outflow reported by Beuther et al. (2002).

Figure 5b presents channel maps of the HCN 1-0 emission. The HCN 1-0 transition has three hyperfine components (F = 1–1, 2–1 and 0–1) at relative frequencies corresponding to 4.8, 0 and −7.1 km s^{-1}, respectively. We set the hyperfine component F = 2−1 at a $V_{\rm LSR}$ of 85.2 km s^{-1}, the cloud systemic velocity. It appears that the emission from the F = 1–1 component is weak. The F = 2–1 and 0–1 components are detected around 80 and 73 km s^{-1}, respectively (see also Fig. 7), 5 km s^{-1} blue shifted from the cloud velocity. The HCN emission arises mainly in two strong peaks: one is associated with the dust peak MM-1, the other is 4″ offset from MM-2 and coincides with the SiO peak in the outflow. Little emission is detected toward MM-2.

The measured flux ratios of the three HCN hyperfine components (F = 0–1, 2–1 and 1–1) amount to 1:1:0.2. Under the LTE condition, line ratios vary from 1:5:3 for optically thin emission to 1:1:1 for optically thick emission. The measured ratios are not consistent with partially optically thick gas under LTE. Anomalous hyperfine ratios of HCN have been found in both cold dark clouds and warm clouds around HII regions (Walmsley et al. 1982; Cernicharo et al. 1984). Possible causes involve overlapping hyperfine components of higher rotational transitions or core-envelope density structures/velocity gradients in the cloud (Gonzalez-Alfonso & Cernicharo 1993). The ratios measured in IRAS 18566+0408 are different from those in dark or warm clouds. Missing short spacing flux in the interferometer data can affect the observed core and envelope emissions differently, which in turn affects the hyperfine ratios. Therefore, we do not further investigate this issue quantitatively.

3.3. Rotational temperature

We derive rotational temperatures of the NH_3 gas. In the calculation, we assumed LTE conditions in the gas and followed the procedure outlined in Ho & Townes (1983). Figure 6 presents a map of rotational temperature derived from the NH_3 (1,1) and (2,2) lines. In most of the core, temperatures are around 10 K to 15 K. Higher rotational temperatures of about 45 K are found toward MM-1, and along the ridge of SiO emission. In this high temperature region, there exists an area where the rotational temperatures cannot be derived. This is because the ratio of the (1, 1) and (2, 2) lines is sensitive to temperatures only up to 50 K (Ho & Townes 1983). At temperatures over 50 K, the ratio of the two lines approaches 1 for the optically thick case, and 1.3 in the optically thin case for a wide range of temperatures. A small error in the flux measurement will result in a large uncertainty

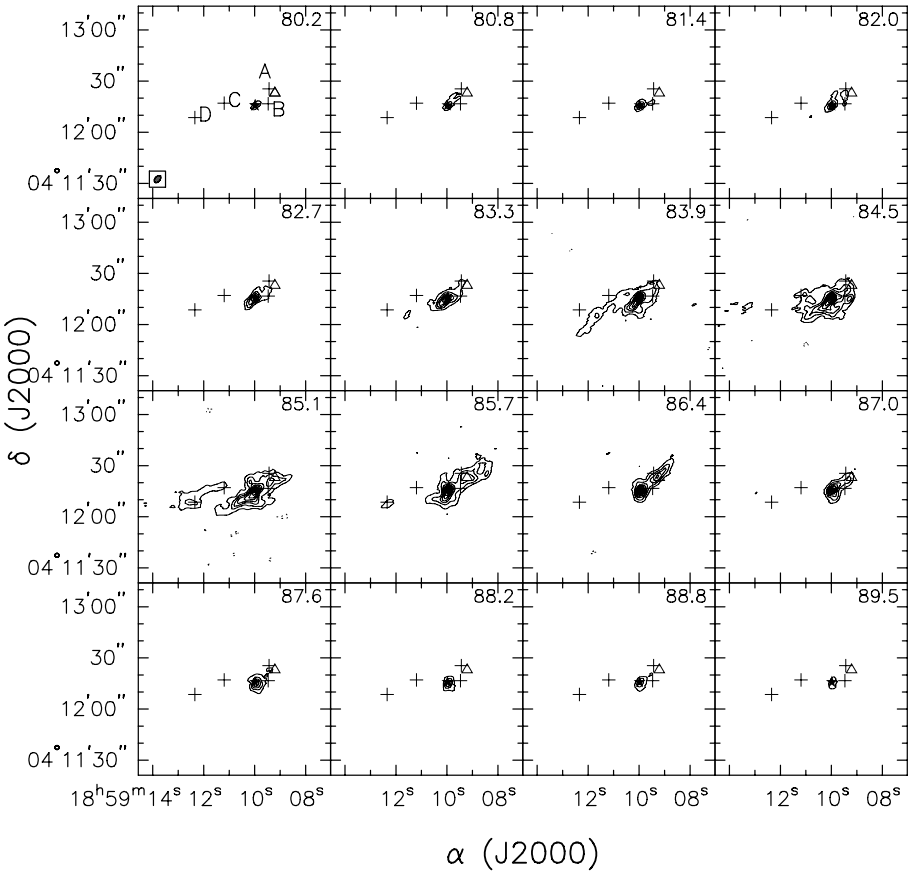

Fig. 4b. continued.

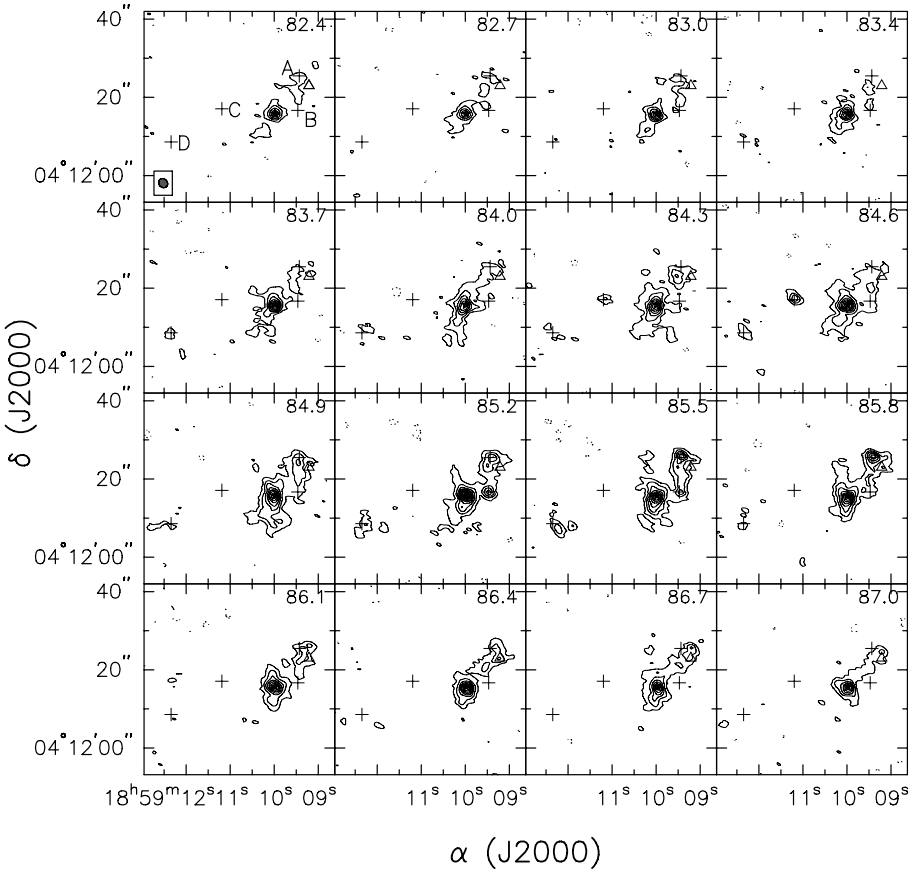

Fig. 4c. continued.

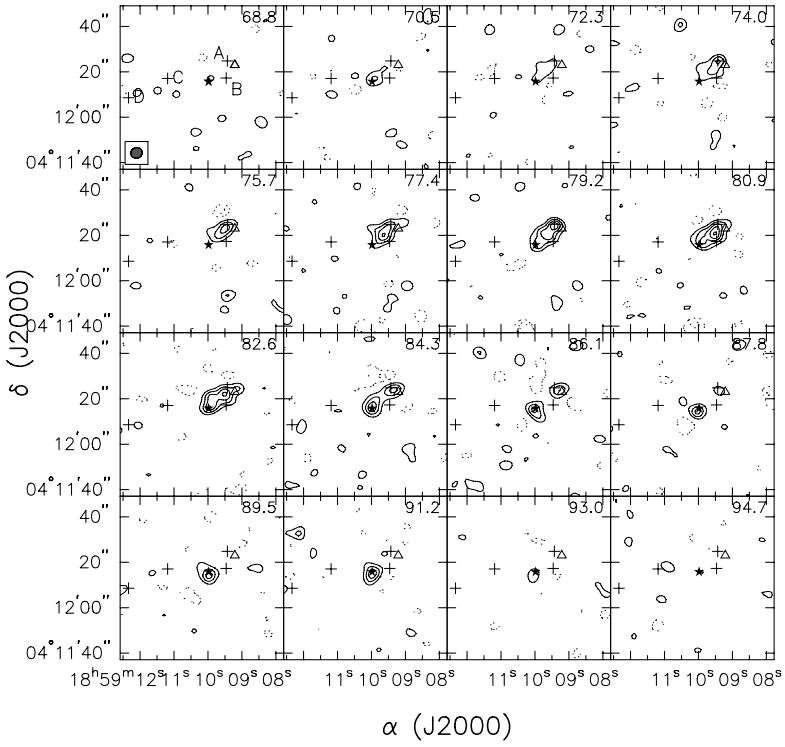

Fig. 5a. The channel maps of the SiO J = (2–1) (Fig. 5a) and HCN J = (1–0) (Fig. 5b) lines. The images were made using the OVRO E configuration data only. The contour levels are in steps of 0.05 Jy/beam for the SiO line, and 0.07 Jy/beam for the HCN line ($\sim 3\sigma$). The beam sizes are plotted at the lower-left of the first panel. The velocity of the channel is plotted at the upper-right of each panel. The "star" symbol and "triangle" mark the continuum peaks MM-1 and MM-2, respectively. The crosses mark the position of the hot NH_3 (3, 3) features.

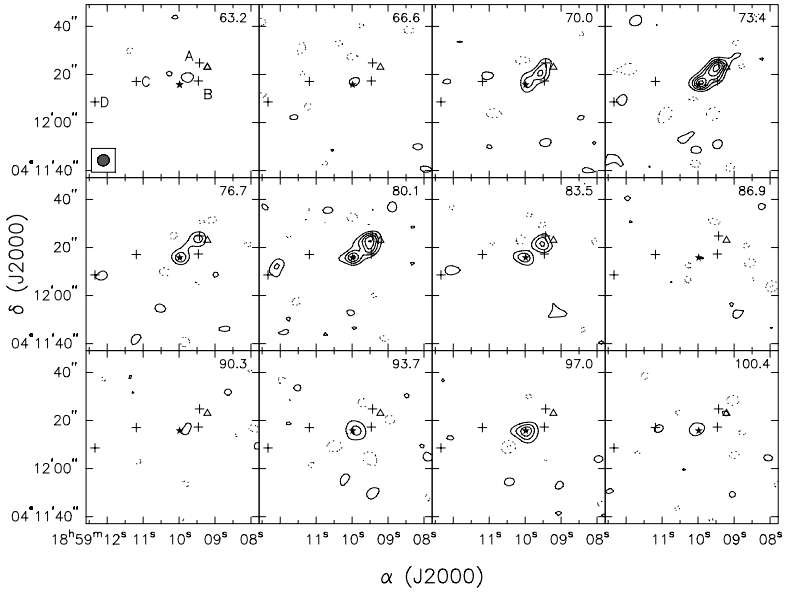

Fig. 5b. continued.

in rotational temperatures. Thus, the blanked area along the SiO outflow in Fig. 6 has even higher temperatures. Assuming the same abundance for the ortho and para NH_3 species, we use the (3, 3) and the (1, 1) lines to obtain a temperature estimate of 70 K for blanked area in the outflow region.

4. Discussions

4.1. Nature of the continuum peaks

The 3 mm continuum emission reveals two peaks, MM-1 and MM-2, bridged by a faint extended filament. The dominant peak MM-1 coincides with the compact 7mm continuum source, faint cm continuum emission (Araya et al. 2005; Carral et al. 1999), and the strong peaks in NH_3, SiO and HCN emission. The rotational temperature estimated from NH_3 is 45 K, corresponding to a kinetic temperature of 80 K (Danby et al. 1988). The luminosity of the internal source required to produce the heating can be estimated by the following equation (Scoville & Kwan 1976)

$$T_{\rm D} = 65 \left(\frac{0.1 \text{ pc}}{r}\right)^{2/(4+\beta)} \left(\frac{L_{\rm star}}{10^5\, L_\odot}\right)^{1/(1+\beta)} \left(\frac{0.1}{f}\right)^{1/(4+\beta)} \text{K}.$$

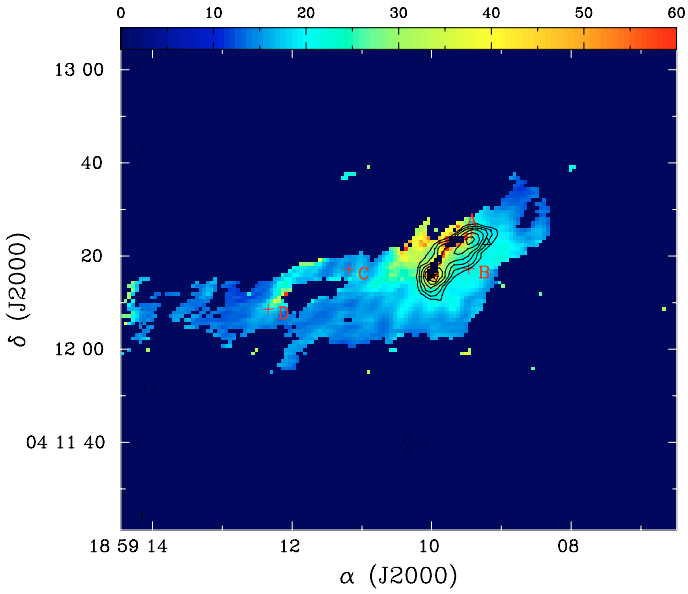

Fig. 6. The color scale shows the rotation temperatures derived from the NH_3 (1, 1) and (2, 2) lines. The contours represent the integrated emission of the SiO 2–1 line. The "star" symbol and "triangle" mark the continuum peaks MM-1 and MM-2, respectively. The crosses mark the position of the hot NH_3 (3,3) features.

Here β is the power law index of the dust emissivity at far infrared wavelengths, $f = 0.08$ cm^2 g^{-1} is the value of the dust emissivity at 50 μm, and r the core radius. If the dust and gas reach a thermal equilibrium in the high density environment, i.e., $T_D = 80$ K at a radius $r = 7000$ AU, and $\beta = 1$, we estimate the luminosity of the embedded source to be 6×10^4 $L_\odot$. This value is in rough agreement with the far IR luminosity observed for the region. The high luminosity, strong dust and molecular line emission, and high temperature in the gas all indicate embedded massive protostar(s) toward MM-1.

The secondary mm peak MM-2 lies in a molecular ridge seen in NH_3 and coincides with a local NH_3 peak in the (1, 1) and (2, 2) transitions (see channels 85.7 and 86.4 km s^{-1} in Figs. 4a and 4b). This molecular ridge appears to correspond to the dust emission seen at 3 mm and 1.2 mm. NH_3 gas temperature toward MM-2 is about 30 K. The large amount of dense molecular gas and a local peak in the gas and dust emission may indicate embedded protostar(s) in the core. If the heating of the gas and dust is due to an internal source, we find a luminosity of 8×10^3 $L_\odot$ for the protostar, through a similar analysis as described above for MM-1. On the other hand, if the heating is partially due to the molecular outflow in the region (see discussions below), the total luminosity for MM-2 would be lower.

4.2. Massive molecular outflow in SiO and NH_3

The SiO emission delineates a bipolar molecular outflow in the region. Figure 7 shows the position-velocity plots of the SiO, HCN, and NH_3 (2, 2) and (3, 3) emissions along the major axis of the SiO emission at a position angle of 135°. Toward the northwest of MM-1, the SiO emission is blue shifted with respect to the cloud systemic velocity of 85.2 km s^{-1}. The terminal velocity of the blue-shifted SiO emission is about 15 km s^{-1} from the cloud velocity. Close to the peak MM-1, both the blue- and red-shifted SiO emissions are detected up to 30 km s^{-1} (3σ level) from the cloud velocity. The blue-shifted SiO emission extends 15″ to the northwest. The red-shifted emission is far more compact spatially, with a peak detected only 2″ southeast of MM-1.

As shown in Fig. 7, there exists cold and quiescent NH_3 gas along the outflow direction. The NH_3 emission peaks at V_{LSR} of 85.2 km s^{-1}, and has a narrow *FWHM* of <2 km s^{-1}. In addition to the cold gas, there exists blue-shifted high velocity emission up to V_{LSR} of 70 km s^{-1}, 15 km s^{-1} from the cloud core velocity. This high velocity gas, offset to the northwest from the continuum peak, is part of the blue-shifted molecular outflow. The gas has an estimated temperature of 70 K. Although NH_3 is a reliable tracer of dense gas in molecular cloud cores, it can be affected by molecular outflows associated with both low and high mass stars (L1157: Tafalla & Bachiller 1995; IRAS20126+4104: Zhang et al. 1999). The high velocity NH_3 and SiO gas has been likely accelerated and heated by shock processes in the outflow.

Although the major axis of the SiO outflow agrees with that of the CO 2–1 outflow obtained at 11″ resolution (Beuther et al. 2002b), the CO outflow exhibits nearly symmetric bipolar morphology with the southeastern lobe much stronger than that in the SiO. Furthermore, the polarity of the SiO outflow appears to be the opposite of that of the CO: the blue-shifted SiO emission lies to the northwest of the star, while the blue-shifted CO emission lies to the southeast of the star. This change of polarity between different tracers has been seen toward other objects (e.g. IRAS 20126+4104; Cesaroni et al. 1997; 1999). One plausible explanation is that the outflow axis lies almost in the plane of the sky and precesses. The low density CO gas traces the wide angle component in the outflow, while the high density SiO gas traces the well collimated jet component in the outflow. On the other hand, CO outflows toward massive star forming regions are often unresolved by single dish telescopes, and break into multiple bipolar outflows at high angular resolution (e.g. I05358, Beuther et al. 2002; AFGL 5142, Zhang et al. 2007). Furthermore, the SiO and CO may trace different outflows as shown in AFGL 5142 (Zhang et al. 2007; Hunter et al. 1999) and the Orion South region (Zapata et al. 2006). High resolution CO images of the outflow will help resolving the difference.

We compute the mass, momentum and energy in the SiO outflow. Using an SiO to H_2 fractional abundance of 10^{-7} (Zhang et al. 1995), an excitation temperature of 70 K derived from NH_3, and assuming optically thin SiO emission, we obtain outflow mass, momentum and energy of 18 $M_\odot$, 200 $M_\odot$ km s^{-1}, and 4.0×10^{46} erg, respectively, in the blue-shifted lobe. Likewise, we obtain 9 $M_\odot$, 70 $M_\odot$ km s^{-1}, and 1.0×10^{46} ergs in the red-shifted lobe. Despite the uncertainty in the SiO abundance, the total mass, momentum and energy of 27 $M_\odot$, 270 $M_\odot$ km s^{-1}, and 5.0×10^{46} ergs are in a rough agreement (within a factor of 2) with the estimates from the CO outflow (Beuther et al. 2002b).

The terminal velocity of 15 km s^{-1} and the length of the SiO outflow (15″) yield a dynamical time scale (T_{dyn}) of 1.7×10^4 years. This value is a few times smaller than that of the CO based on the lower angular resolution data (Beuther et al. 2002b). Assuming momentum conservation between the outflow and the underlying wind that powers the outflow: $m_w V_w = P_{outflow}$, we can estimate the mass loss rate in the wind over the dynamical time scale of the outflow. The wind velocity V_w can vary from 100 km s^{-1} in low-mass stars to 500 km s^{-1} in high-mass stars (Zhang et al. 2005). Since the effect of inclination angle of the outflow is not corrected, we use a lower value of 100 km s^{-1} for the wind velocity. This gives a mass loss rate (m_w/T_{dyn}) of 1.5×10^{-4} $M_\odot$ yr^{-1}, and thus a lower limit to the mass accretion rate of 1.5×10^{-4} $M_\odot$ yr^{-1}, since some material presumably goes into the central protostar (Churchwell 2002).

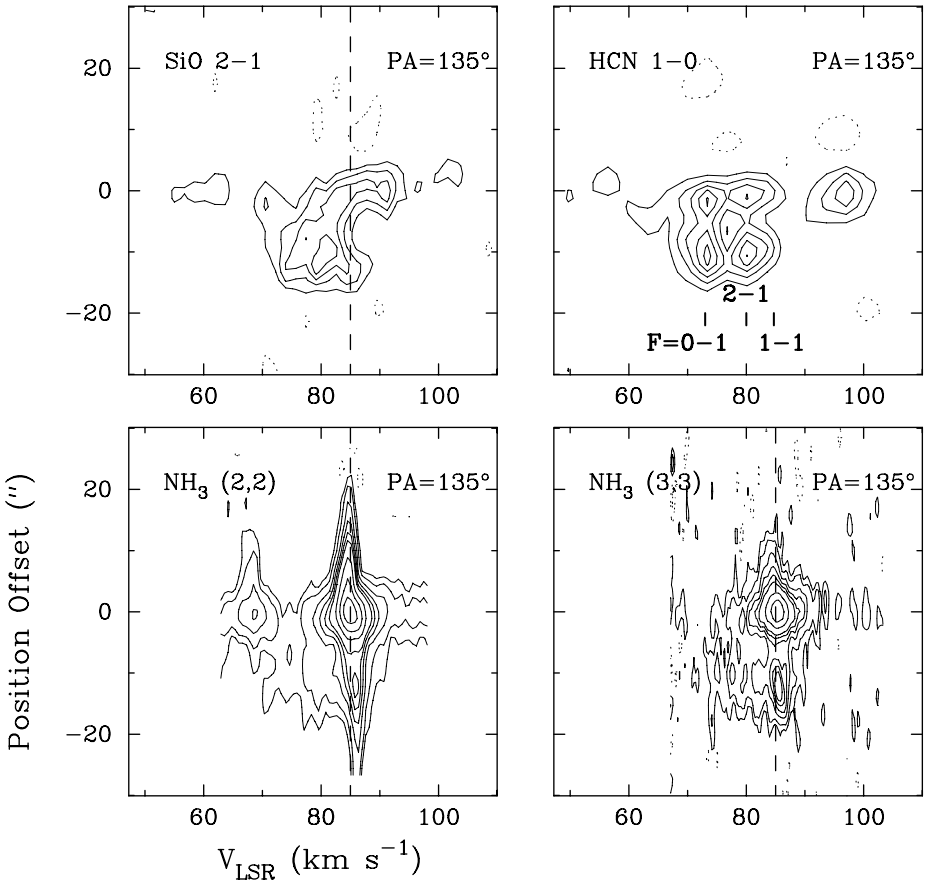

Fig. 7. The position-velocity plots of the SiO 2–1, HCN 1–0, NH_3 $(J, K) = (1, 1), (2, 2)$ and $(3, 3)$ lines. The abcissa is offset from the position of the dust continuum with position angle (PA) of 135°. The positive offset represents the southeast of the dust continuum peak. The contours for the SiO and HCN are plotted in steps of ±0.05 Jy/beam for the SiO line, and ±0.07 Jy/beam for the HCN line ($\sim 3\sigma$), respectively. The NH_3 data are contoured at $3 \times (1, 2, 4, 6, 8, 10, 15, 20, 25)$ mJy/beam. The three HCN hyperfine components are labeled assuming a cloud systemic velocity of 85.2 km s^{-1}. The NH_3 $(2, 2)$ emission around 72 km s^{-1} is the satellite hyperfine component.

4.3. Heating and weak maser emission

The outflow apparently causes significant heating in the molecular gas, especially toward the blue-shifted lobe. As shown in Fig. 6, the rotational temperature derived from the NH_3 $(1, 1)$ and $(2, 2)$ lines is 45 K toward the position of MM-1. However, the temperature in the outflowing gas toward the blue-shifted lobe is higher, with values of 50–70 K.

The effect of heating is further demonstrated in Fig. 8. We compute ratios of the NH_3 $(3, 3)$ and $(1, 1)$ emission. As the $(3, 3)$ transition has an energy level of 124 K, the higher ratios in general represent higher gas temperatures for thermal emission. As shown in Fig. 8, the NH_3 gas in the outflow region exhibits consistently higher line ratios, as expected from high temperature regions. Toward the positions "C" and "D", there appears to be heated NH_3 gas in a bow shape. The NH_3 spectrum toward "C" shows red-shifted line wings, while the NH_3 spectra toward "D" show blue-shifted line wings. Furthermore, the tips of the bows point away from each other, as seen in the upper-right panel in Fig. 8. It is possible that the heating in NH_3 traces another outflow, which is not seen in SiO. The heating likely arises from bow shocks as high velocity gas impinges on the cloud core. The potential driving source should lie in between "C" and "D". However, no dust continuum emission is detected at a 3σ limit of 4 $M_\odot$.

Figure 9 presents NH_3 spectra toward positions "A", "B", "C" and "D". All NH_3 spectra display line wing emission 15 km s^{-1} blue shifted from the cloud velocity. Toward "A", "B" and "C", the $(3, 3)$ line has a *FWHM* of <1.5 km s^{-1}, smaller than the ~3 km s^{-1} *FWHM* in the $(1, 1)$ and $(2, 2)$ lines. The compact morphology, the narrow linewidth, and a lack of corresponding peaks in the NH_3 $(1, 1)$ and $(2, 2)$ emission indicate that the compact $(3, 3)$ emission arises from population inversion, similar to maser emission. Maser inversion of the NH_3 $(3, 3)$ has been detected toward a number of sources (e.g. W51, Zhang & Ho 1995, NGC 6334, Kraemer & Jackson 1995; Beuther et al. Beuther2007; DR 21(OH), Mangum & Wootten 1994; Mauersberger et al. 1986; IRAS 20126+4104, Zhang et al. 2001). NH_3 $(3, 3)$ inversion can form through collisional excitation of NH_3 by H_2 (Walmsley & Ungerechts 1983). Through collisions with H_2, the upper level of the NH_3 $(3, 3)$ (denoted as NH_3 $(3, 3)^+$) exchanges with its $(0, 0)$ state while the lower level of the $(3, 3)$ exchanges with the $(1, 0)$. Since the transition between the $(3, 3)^+$ and $(0, 0)$ involves a change of parity and thus is more preferred, the $(3, 3)^+$ state can be overpopulated.

NH_3 $(3, 3)$ masers are often observed in outflows. In the cases of IRAS 20126+4104 and NGC 6334 (Kraemer & Jackson 1995; Zhang et al. 2001), $(3, 3)$ masers are detected in the vicinity of bow shocks where outflow wind interacts with the cloud gas. The high velocity NH_3 gas detected toward "A", "B" and "C" (see Fig. 9) suggest a similar scenario. However, the spatially compact NH_3 $(3, 3)$ emission appears to be resolved at an resolution of 1″, suggesting that the emission is not strongly amplified.

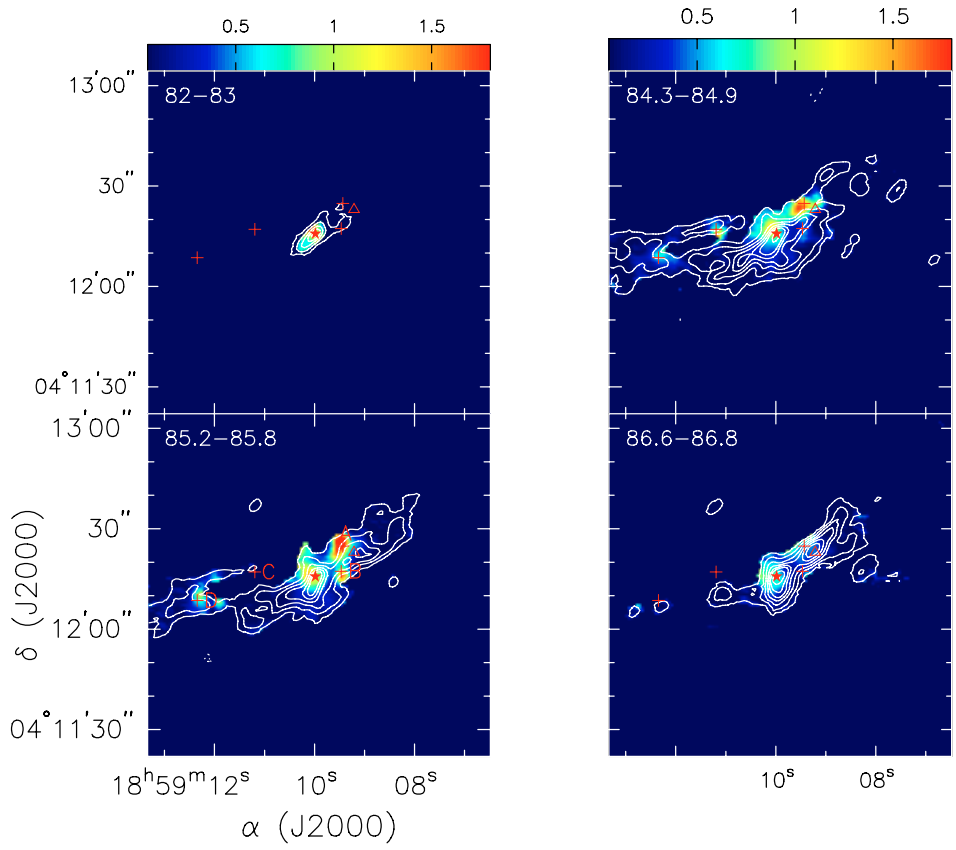

Fig. 8. The ratio of the integrated NH_3 emission (3, 3)/(1, 1) (color) overlaid on the integrated emission of the NH_3 $(J, K) = (1, 1)$ line (contours). The velocity range of the integration in units of km s^{-1} is given at the upper left corner of each panel. The "star" symbol and "triangle" mark the continuum peaks MM-1 and MM-2, respectively. The crosses marks the position of hot NH_3 (3, 3) features.

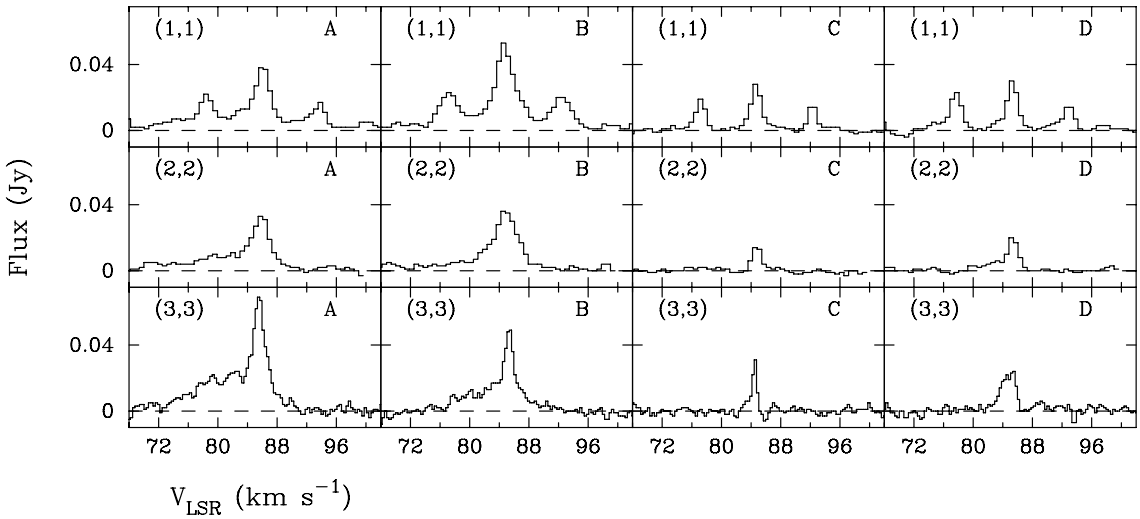

Fig. 9. Spectra of the NH_3 $(J, K) = (1, 1), (2, 2)$ and $(3, 3)$ transitions from the compact components A, B, C, and D.

4.4. Kinematics in the NH_3 core

In MM-1, the compact NH_3 emission with a Gaussian-like profile and large linewidth distinguishes itself from the relatively smooth NH_3 emission in the cloud core. The NH_3 emission toward this position has much broader linewidth: 5.5 km s^{-1} at a spatial resolution of 3″. We image the visibility data from the VLA C array only and obtain an angular resolution of 1″. From this image, we obtain a fitted *FWHM* of 8.7 km s^{-1} in the (3,3) line. This increase indicates additional broadening in the spectral lines towards the inner part of the NH_3 core. The NH_3 compact structure has a size of 1.2″ or 8000 AU. We estimate the mass in this compact structure following Ho & Townes (1983). With a rotational temperature of 45 K, size of 1.2″ and $[\frac{NH_3}{H_2}] = 10^{-7}$ (Harju et al. 1993), and the assumption of LTE, we obtain a mass of 60 $M_\odot$. This value is consistent with the mass estimated from the dust emission.

The broad NH_3 linewidth toward MM-1 can arise from outflow, infall/rotation or relative motion of multiple objects

unresolved within the synthesized beam. A collimated molecular outflow is present in the SiO emission with high velocity emission toward the northwest and the southest of MM-1. The effect of the outflow also appears in the NH_3 emission, especially toward the northwest of MM-1 along the outflow lobe. Can the molecular outflow produce the line broadening seen in NH_3 toward MM-1? The SiO emission is shifted from the cloud velocity. On the contrary, the NH_3 emission peaks mostly at the cloud velocity and appears to be Gaussian in profile. Furthermore, the mass and momentum in the outflow within the $5\farcs0 \times 4\farcs7$ area (the synthesized beam of the SiO data) of MM-1 are 1.5 $M_\odot$ and 10 $M_\odot$ km s^{-1}, respectively. Similarly, we compute the same quantities from the NH_3 gas over a scale of $1\farcs2$, and find the mass and momentum of 60 $M_\odot$ and 250 $M_\odot$ km s^{-1}, respectively. The fractional abundances of NH_3 and SiO may be uncertain and thus can affect the estimates provided above. Nevertheless, the comparison between the masses in SiO and NH_3 shows that toward the most central region of the core only <3% of the material traced by the NH_3 emission is from the molecular outflow. Since the outflow mass is calculated over the area ($5\farcs0 \times 4\farcs7$) 15 times larger than that of the NH_3 emission, the actual contribution from the outflow can be even smaller. Thus, it is unlikely that the molecular outflow is the main contributor to the NH_3 linewidth.

The remaining possibilities for the large NH_3 linewidth are motions such as infall/rotation or relative motion of multiple cores within the synthesized beam. Higher angular resolution observations in dust continuum and spectral lines will be fruitful in distinguishing these possibilities. If the NH_3 linewidths are due to rotation and infall, similar to the signature seen in NH_3 toward IRAS 20126+4104 (Zhang et al. 1998), the dynamical mass, assuming gravitationally bound motion, derived using $M = \frac{V_{\rm rot}^2 R}{2G}$, is 35 $M_\odot$, for $V_{\rm rot}$ = 3 km s^{-1} at R = 7000 AU. This is compatible with the mass estimate from dust emission and NH_3 at a similar scale. The mass infall rate, estimated using $4\pi R^2 n_{\rm H_2} V_{\rm infall}$, is 1.5×10^{-3} $M_\odot$ yr^{-1} for $V_{\rm infall}$ = 3 km s^{-1} and $n_{\rm H_2} = 10^6$ cm^{-3}. Thus, the mass loss rate in the wind, $1.5{\times}10^{-4}$ $M_\odot$ yr^{-1} (Sect. 4.2), is 10% of the infall rate. Assuming that 10% to 30% of the infalling mass is ejected in the outflow, the accretion luminosity, estimated from $\frac{GM\dot{M}}{r}$, amounts to 3–4 $\times 10^4$ $L_\odot$, about half of the far-IR luminosity.

5. Conclusion

We conducted observations of the high-mass protostellar candidate IRAS 18566+0408 with the VLA and OVRO interferometers.

(1) We resolve a collimated outflow in SiO (2-1) emission. The outflow is also detected in the line wings of NH_3 inversion transitions and produces significant heating of the molecular gas (up to 70 K). Compact features in the NH_3 (3, 3) line are detected along the outflow. The narrow linewidths of <1.5 km s^{-1} suggest that they are weakly amplified maser emission.

(2) The 87 GHz emission reveals two peaks MM-1 and MM-2. The internal heating in the MM-1 core calls for embedded massive young star(s). The NH_3 linewidth toward MM-1 is much broader than the typical linewidth of <2 km s^{-1} in the extended core, and increases inward from 5.5 km s^{-1} at the $3''$ scale to 8.7 km s^{-1} at the $1''$ scale. The motion is consistent with rotation/infall, but can also arise from relative motions of unresolved protostellar cores.

Acknowledgements. We appreciate Editor M. Walmsley for his valuable comments. H. B. acknowledges financial support by the Emmy-Noether-Programm of the Deutsche Forschungsgemeinschaft (DFG, grant BE2578). Y. C. thanks the support by the NSFC Grant 110133020.

References

Araya, E., Hofner, P., Kurtz, S., et al. 2005, ApJ, 618, 339
Bachiller, R. 1996, ARA&A, 34, 111
Bachiller, R., Martín-Pintado, J., & Fuente, A. 1993, ApJ, 417, L45
Beltrán, M. T., Brand, J., Cesaroni, R., et al. 2006, A&A, 447, 221
Beuther, H., Schilke, P., Menten, K. M., et al. 2002a, ApJ, 566, 945
Beuther, H., Schilke, P., Sridharan, T. K., et al. 2002b, A&A, 383, 892
Beuther, H., Walsh, A., Schilke, P., et al. 2002c, A&A, 390, 289
Beuther, H., Schilke, P., Gueth, F., et al. 2002d, A&A, 387, 931
Beuther H., Hunter, T.R., Zhang, Q., et al. 2004, ApJ, 616, L23
Beuther, H., Zhang, Q., Sridharan, T. K., & Chen Y. 2005, ApJ, 628, 800
Bronfman, L., Nyman, L.-A., & May, J. 1996, ApJS, 71, 481
Burke, J. R., & Hollenbach, D. J. 1983, ApJ, 265, 223
Carral, P., Kurtz, S., Rodríguez, L. F., et al. 1999, RMxAA, 35, 97
Cernicharo, J., Castets, A., Duvert, G., & Guilloteau, S. 1984, A&A, 139, L13
Cesaroni, R., Felli, M., Testi, L., Walmsley, C. M., & Olmi, L. 1997, A&A, 325, 725
Cesaroni, R., Felli, M., Jenness, T., et al. 1999, A&A, 345, 949
Cesaroni, R., Neri, R., Olmi, L., et al. 2005, A&A, 434, 1039
Churchwell, E. 2002, Hot Star Workshop III: The Earliest Phases of Massive Star Birth, 267, 3
Fontani, F., Beltrán, M. T., Brand, J., et al. 2005, A&A, 432, 921
Gonzalez-Alfonso, E., & Cernicharo, J. 1993, A&A, 279, 506
Harju, J., Walmsley, C. M., & Wouterloot, J. G. A. 1993, ApJS, 98, 51
Hildebrand, R. H. 1983, QJRAS, 24, 267
Ho, P. T. P., & Townes, C. H. 1983, ARA&A, 21, 239
Hunter, T. R., Testi, L., Zhang, Q., & Sridharan, T. K. 1999, AJ, 118, 477
Kraemer, K. E., & Jackson, J. M. 1995 ApJ, 439, L9
Mangum, J. G., & Wootten, A. 1994, ApJ, 433, L134
Mauersberger, R., Wilson, T. L., & Henkel, C. 1986, A&A, 160, L13
McCutcheon, W. H., Dewdney, P. E., Purton, R., & Sato, T. 1991, AJ, 101, 1435
Madden S. C., Irvine W. M., Matthews H. E., Brown R. D., & Godfrey P. D. 1986, ApJ, 300, L79
Miralles, M. P., Rodríguez, L. F., & Scalise, E. 1994, ApJS, 92, 173
Molinari, S., Brand, J., Cesaroni, R., & Palla, F. 1996, A&A, 308, 573
Osterloh, M., Henning, Th., & Launhardt, R. 1997, ApJS, 110, 71
Pineau des Forêts, G., Flower, D. R., & Chièze, J.-P. 1997, in Herbig-Haro Flows and the Birth of Low Mass Stars, ed. B. Reipurth, & C. Dertout (Dordrecht: Kluwer), 199
Sako, S., Yamashita, T., Kataza, H., et al. 2005, Nature, 434, 995
Shepherd, D. S., & Churchwell, E. 1996, ApJ, 472, 225
Shepherd, D.S., Claussen, M.J., & Kurtz, S. 2001, Science, 292, 1513
Slysh, V. I., Val'tts, I. E., Kalenskii, S. V., et al. 1999, A&AS, 134, 115
Scoville, N. Z., & Kwan, J. 1976, ApJ, 206, 718
Sridharan, T. K., Beuther, H., Schilke, P., Menten, K. M., & Wyrowski, F. 2002, ApJ, 566, 931
Walmsley, C. M., & Ungerechts, H. 1983, A&A, 122, 164
Walmsley, C. M., Churchwell, E., Nash, A., & Fitzpatrick, E. 1982, ApJ, 258, L75
Williams, S. J., Fuller, G. A., & Sridharan, T. K. 2004, A&A, 417, 115
Wilking, B. A., Mundy, L. G., Blackwell, J. H., & Howe, J. E. 1989, ApJ, 345, 257
Wu, J., & Evans, N. J., II 2003, ApJ, 592, L79
Zapata, L. A., Rodríguez, L. F., Ho, P. T. P., et al. 2005, ApJ, 630, L85
Zhang, Q., & Ho, P. T. P. 1995, ApJ, 450, L63
Zhang, Q., Hunter, T. R., & Sridharan, T. K. 1998, ApJ, 505, L154
Zhang, Q., Hunter, T. R., Sridharan, T. K., & Cesaroni, R. 1999, ApJ, 527, L117
Zhang, Q., Hunter, T. R., Brand, J., et al. 2001, ApJ, 552, L167
Zhang, Q., Hunter, T.R., Sridharan, T.K., & Ho, P. T. P. 2002, ApJ, 566, 982
Zhang, Q., Hunter, T. R., Brand, J., et al. 2005, ApJ, 625, 864
Zhang, Q., Hunter, T. R., Beuther, H., et al. 2007, ApJ, 658, 1152
Ziurys, L. M., Friberg, P., & Irvine, W. M. 1989, ApJ, 343, 201